SUPPORTING INFORMATION

Key-to-Lock Halogen Bond-Based Tetragonal Pyramidal Association of Iodonium Cations with the Lacune Rims of Beta-Octamolybdate

Natalia S. Soldatova,[1] Amirbek D. Radzhabov,[1] Daniil M. Ivanov,[1,2] Sergi Burguera,[3] Antonio Frontera,[3] Pavel A. Abramov,[1,4]* Pavel S. Postnikov,[1,5]* and Vadim Yu. Kukushkin[2,6]*

1. Research School of Chemistry and Applied Biomedical Sciences, Tomsk Polytechnic University, Tomsk 634050, Russian Federation
2. Institute of Chemistry, Saint Petersburg State University, Universitetskaya Nab. 7/9, Saint Petersburg 199034, Russian Federation
3. Department of Chemistry, Universitat de les Illes Balears, Crta. de Valldemossa km 7.5, 07122 Palma de Mallorca (Baleares), Spain
4. Nikolaev Institute of Inorganic Chemistry SB RAS, 3 Acad. Lavrentiev Av., Novosibirsk, 630090, Russian Federation
5. Department of Solid State Engineering, Institute of Chemical Technology, Prague 16628, Czech Republic
6. Institute of Chemistry and Pharmaceutical Technologies, Altai State University, 656049 Barnaul, Russian Federation

Table of contents:

Table S1. Lengths (d) and angles (φ) of halogen bonds with polyoxometalate anions

Compound	Contact	d, Å	φ, °	Reference
(2-IpyH)$_3$(2-Ipy)[PMo$_{12}$O$_{40}$]·3EtOH	C6–I2···O31	3.136(5)	167.8(2)	Ref.[1]
	C11–I3···O15	3.002(3)	172.2(5)	
(3-IpyH)$_3$(3-Ipy)$_2$[PMo$_{12}$O$_{40}$]·H$_2$O	C2–I1···O1	3.243(4)	170.1(8)	
	C17–I4···O12	3.326(5)	167.9(3)	
	C12–I3···O28	3.382(7)	155.1(4)	
	C12–I3···O35	3.262(5)	159.4(3)	
	C22–I5···O8	3.136(2)	165.9(4)	
(4-IpyH)$_3$[PMo$_{12}$O$_{40}$]·EtOAc·H$_2$O	C3–I1···O44	3.195(6)	168.5(6)	
	C13–I3···O8	3.496(6)	171.8(6)	
(4-IpyH)$_3$[PMo$_{12}$O$_{40}$]	C3–I1···O10	3.317(8)	166.7(4)	
(3-IpyEt)$_4$[PMo$_{12}$O$_{40}$]	C2–I1···O16	3.029(2)	167.3(2)	
	C9–I2···O34	3.098(2)	165.2(2)	
	C16–I3···O4	2.986(2)	169.2(9)	
	C23–I4···O27	3.055(1)	168.0(9)	
(3-BrpyEt)$_4$[PMo$_{12}$O$_{40}$]	C2–Br1···O1	3.233(3)	164.7(8)	
	C9–Br2···O28	2.944(6)	163.1(9)	
	C16–Br3···O4	3.117(4)	149.5(9)	
(35-BrpyEt)$_3$[PMo$_{12}$O$_{40}$]·4.5DMSO	C2–Br1···O39	3.130(4)	170.3(3)	
	C4–Br2···O22	3.185(3)	173.7(7)	
	C18–Br6···O24	3.316(2)	167.4(7)	
[(3IPy)$_2$Bu]$_2$[PMo$_{12}$O$_{40}$]Br	C11–I2···O19	3.296(5)	161.8(7)	
[(3IPy)$_2$Bu]$_2$[PMo$_{12}$O$_{40}$]·2DMSO	C2–I1···O10	3.114(2)	157.6(2)	
	C9–I2···O6	3.279(9)	153.9(5)	
[(3-IpyEt)$_2$(3-IpyH)][PW$_{12}$O$_{40}$]·DMSO	C2–I1···O17	3.413(5)	161.7(3)	
	C9–I3···O33	3.038(3)	168.8(9)	
(Bu$_4$N)$_2$[β-{Ag(py–Cl)}$_2$Mo$_8$O$_{26}$]	C4–Cl1…O6	3.252(5)	175.5(2)	Ref.[2]
(Bu$_4$N)$_2$[β-{Ag(py–Br)}$_2$Mo$_8$O$_{26}$]	C24–Br1…O3	3.197(5)	173.9(2)	
(Bu$_4$N)$_2$[β-{Ag(py–I)}$_2$Mo$_8$O$_{26}$]	C4–I1…O1	3.217(5)	171.5(2)	
(TBA)$_3$[MnMo$_6$O$_{18}${(OCH$_2$)$_3$CNHCO(C$_6$H$_4$-p-I)}$_2$]	C9–I1…O3	3.045(5)	167.5(2)	Ref.[3]
(Ph$_2$I)$_4$[Mo$_8$O$_{26}$]·3DMF·H$_2$O	C43–I4…O31	2.933(5)	170.0(2)	Ref.[4]
	C7–I1…O19	2.908(5)	168.5(2)	
	C19–I2…O39	3.242(5)	159.0(2)	
	C13–I2…O42	2.830(5)	174.7(2)	
	C31–I3…O4	2.973(5)	168.1(2)	
	C25–I3…O6	2.821(5)	165.3(2)	
[MoO$_2$(SMB)(py)][a]	C2–I1…O4	3.132(5)	167.7(2)	Ref.[5]
MoO$_2$(SMB)(3-pic)][a]	C2–I1…O5	3.282(5)	165.6(2)	
[MoO$_2$(DSMB)(H$_2$O)](DMF)$_2$[b]	C4–I2…O5	3.061(5)	172.5(2)	Ref.[6]
[MoO$_2$(DSMB)(py)][b]	C2–I1…O5	3.114(5)	165.4(2)	
{(C$_7$H$_{10}$N)$_2$[Mo$_5$O$_{16}$]}$_n$	C1–I1…O8	3.129(5)	167.7(2)	Ref.[7]

[a] H$_2$SMB = 3,5-diiodosalicylaldehyde-4-methoxybenzoylhydrazone; [b] H$_2$DSMB = 3,5-diiodosalicyaldehyde-4-methoxybenzoylhydrazone

Section S1. Chalcogen bond with DMSO

In the structure of 2^{II}, the S1S atom of DMSO interact with O1C atom of the lacune rim to give noncovalent contacts, which belong to the chalcogen bonding category accordingly to the IUPAC criteria[8] (d(S1S···O1C) = 3.189(2) Å; the sum of Bondi vdW radii Σ_{vdW} S + O = 3.32 Å; Nc = 0.96, ∠O1S–S1S···O1C = 172.18(15) Å) and also with the I^{III} site to give weak XB (d(I1D···S1S) = 3.6728(11) Å; the sum of Bondi vdW radii Σ_{vdW} I + S = 3.78 Å; Nc = 0.97, ∠C1D–I1D···S1S = 150.16(10) Å). In this case, the O1C atom of the lacune rim functions as a NCI acceptor for the synergetic chalcogen bonding and XB.[9]

As described above, the DMF and DMSO molecules also form XB and chalcogen bonding (ChB) interactions. Both have been also analyzed herein and the results are gathered in Figures A and B for the XBs and C for the ChB. The XB complex with DMSO (compound **2**, **Figure A**) is characterized by a BCP, bond path and blue RDG isosurface, confirming the existence and strong nature of the XB. An additional BCP and bond path connect one H-atom of the DMSO molecule to one C-atom of the phenyl ring. The size and shape of the RDG isosurface that characterizes this contact suggests that this can be classified as a CH···π interaction. The XB energy derived from the V_b value is –8.0 kcal/mol, comparable to the values found for the strongest and most directional anion···cation XBs described above. The NBO analysis Figure A(b,c) also demonstrates the existence of the typical LP(O) →σ*(C–I) donor-acceptor interactions involving two LPs at the O-atom with concomitant stabilization energies of E(2) = 2.75 and 2.27 kcal/mol.

The XB complex with DMF (compound **3**, Figure B) is characterized by a BCP, bond path and blue RDG isosurface, confirming the existence and strong nature of the XB. The interaction energy derived from the V_b value is –6.8 kcal/mol, slightly weaker than that of the DMSO. The NBO analysis Figure B(b) also demonstrates the existence of the typical LP(O) →σ*(C–I) donor-acceptor interaction with a concomitant stabilization energy of E(2) = 5.61 kcal/mol, that is comparable to the total contribution of the DMSO complex in **2**.
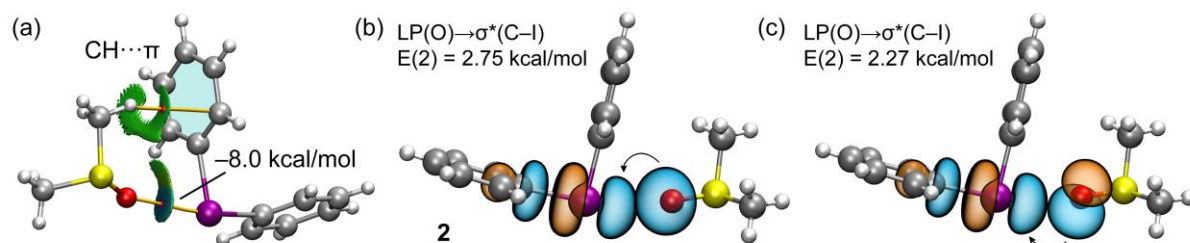
Figure S1. (a) Combined QTAIM (BCPs in red and bond path as solid orange lines) and NCIPlot analysis (RDG = 0.5, ρ cut-off = 0.04, color range –0.04 a.u. ≤ (signλ₂)*ρ ≤ 0.04 a.u. of the DMSO dimer in **2**. The total I···O energy derived from the Vb value is indicated. Only intermolecular interactions are represented. (b,c) NBOs involved in the XB. The second order perturbation energies, E(2), are also given.
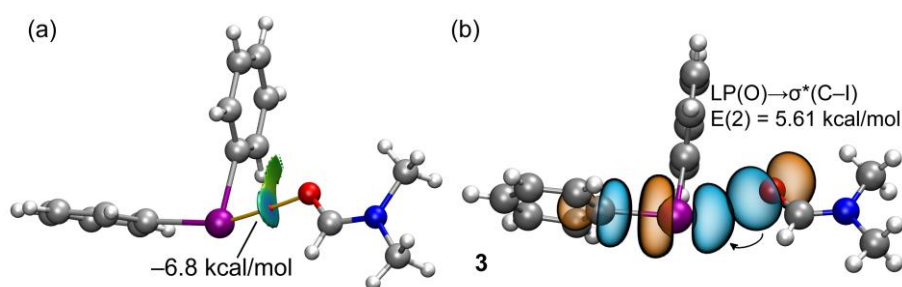

Figure S2. (a) Combined QTAIM (BCPs in red and bond path as solid orange lines) and NCIPlot analysis (RDG = 0.5, ρ cut-off = 0.04, color range –0.04 a.u. ≤ (signλ₂)*ρ ≤ 0.04 a.u. of the DMF dimer in **3**. The total I···O energy derived from the Vb value is indicated. Only intermolecular interactions are represented. (b) NBOs involved in the XB. The second order perturbation energy, E(2), is given.

Finally, the possible role of DMSO as ChB donor (**Figure 2C** in **section 2.1**) was analyzed and the results are gathered in **Figure C**. The combined QTAIM/NCIplot analysis confirms the existence of the S···O contact in cooperation with several CH···O HBs. All contacts are characterized by the corresponding BCPs, bond paths and green isosurfaces. In this case the contribution of the HBs is larger (–4.5 kcal/mol) than that of the chalcogen bond (–1.4 kcal/mol). The NBO analysis also confirms the σ-hole nature of the interaction disclosing a very modest LP(O)→σ(S–O) charge transfer with a stabilization energy of E(2) = 0.32 kcal/mol, in line with the modest ability of sulfur to act as σ-hole donor.

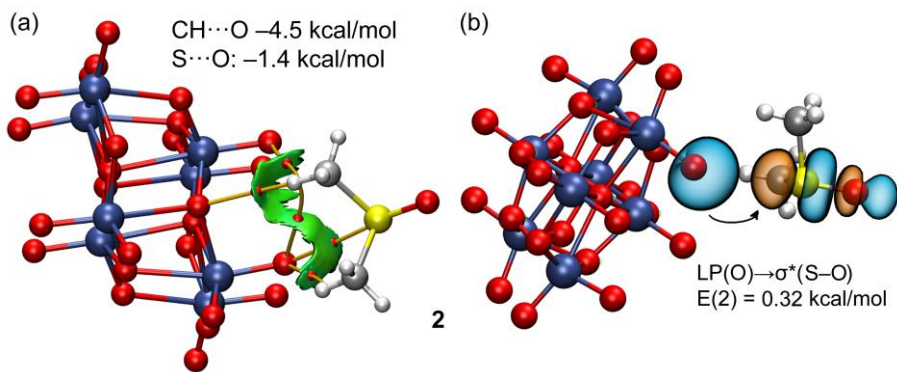(a) CH···O –4.5 kcal/mol
S···O: –1.4 kcal/mol

(b)

LP(O)→σ*(S–O)
E(2) = 0.32 kcal/mol

2

Figure S3 (a) Combined QTAIM (BCPs in red and bond path as solid orange lines) and NCIPlot analysis (RDG = 0.5, ρ cut-off = 0.04, colour range –0.04 a.u. $\leq$ (signλ_2)*ρ $\leq$ 0.04 a.u. of the DMSO···anion dimer in compound **2**. The total CH···O ad S···O energies derived from the V_b values are indicated. Only intermolecular interactions are represented. (b) NBOs involved in the ChB. The second order perturbation energies, E(2), are also given.

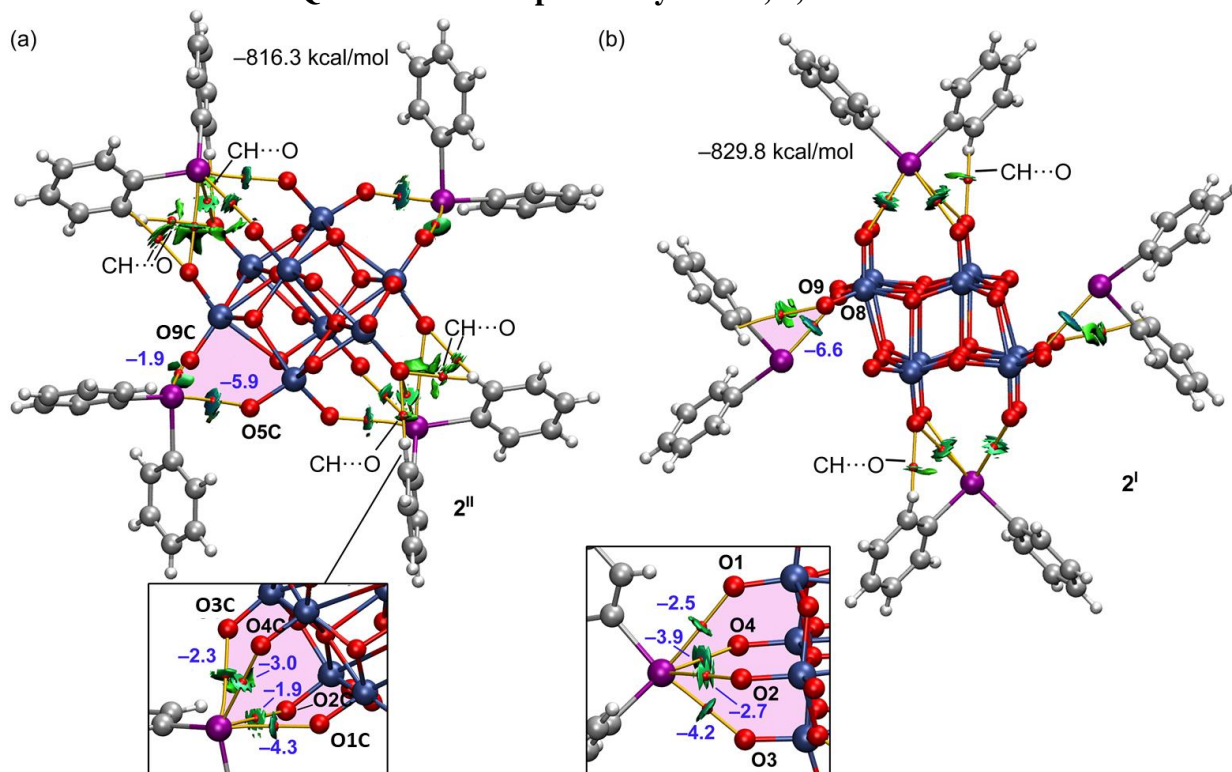## Section S2. Combined QTAIM and NCIplot analysis of 2, 4, and 5

Figure S4. Combined QTAIM (BCPs in red and bond path as solid orange lines) and NCIplot analysis (RDG = 0.5, ρ cut-off = 0.04, color range -0.04 a.u. $\leq$ (signλ_2)*ρ $\leq$ 0.04 a.u. of the pentameric assembly of compounds 2^{II} (a) and 2^{I}. The individual contributions of the XBs are indicated in blue adjacent to the BCPs. Only intermolecular interactions are represented.
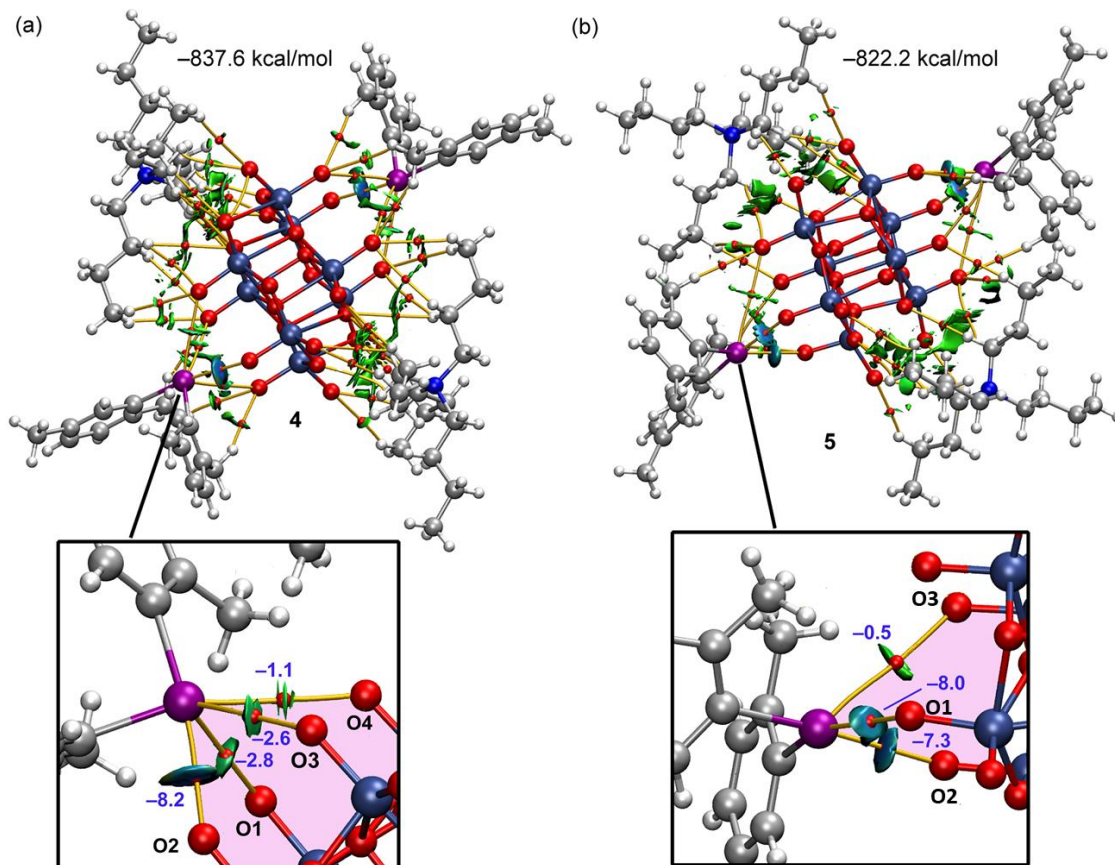
Figure S5. Combined QTAIM (BCPs in red and bond path as solid orange lines) and NCIplot analysis (RDG = 0.5, ρ cut-off = 0.04, color range -0.04 a.u. $\leq$ (signλ_2)*ρ $\leq$ 0.04 a.u. of the pentameric assemblies of compounds **4** (a) and **5** (b). The interaction energy is also indicated. The individual contributions of the XBs are indicated in blue adjacent to the BCPs. Only intermolecular interactions are represented.

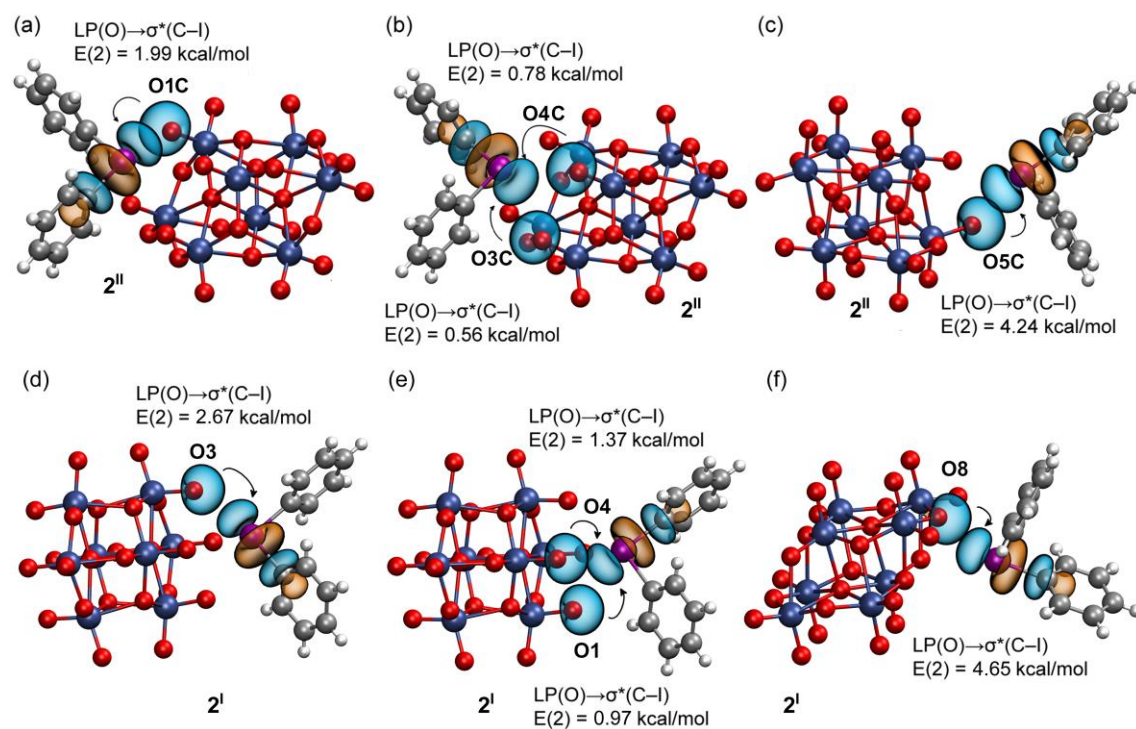## Section S3. NBOs involved in the XBs observed in 2, 4, and 5

Figure S6. NBOs involved in the XBs observed in compound **2^{II}** (top panel) and **2^{I}** (lower panel) for the tetrafurcated (a,b,d,e) and bifurcated (c,f) binding modes. The second order perturbation analysis energies are also given, E(2).
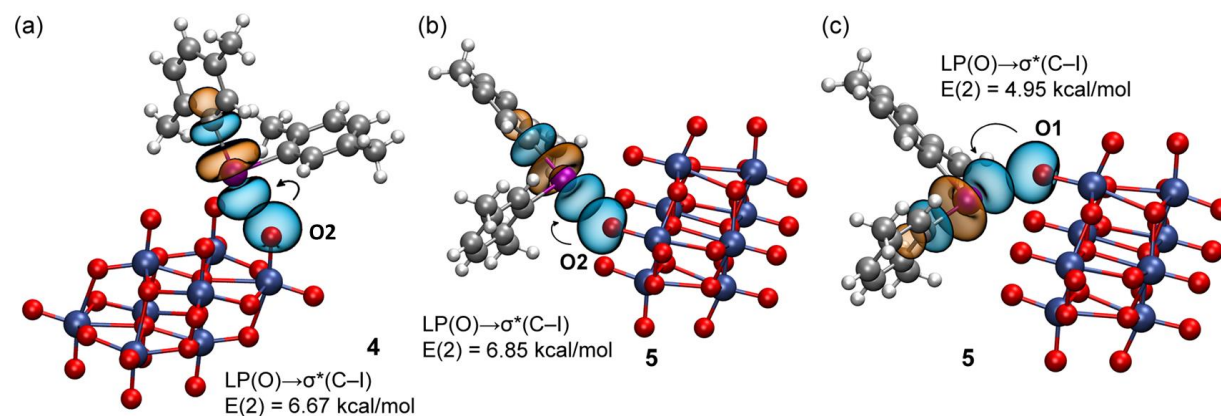

Figure S7. NBOs involved in the XBs observed in compound **4** (a) and **5** (b,c) compounds. The second order perturbation analysis energies are also given, E(2).

Section S4. MEP surface of [Mo$_8$O$_{26}$]$^{4-}$ isomers

MEP surface calculations performed for α, β, γ, and δ-[Mo$_8$O$_{26}$]$^{4-}$ isomeric anions (**Figure S8**) and it was revealed that the non-lacunar α, γ, and δ-[Mo$_8$O$_{26}$]$^{4-}$ anions[10] exhibit $V_{s,min}$ values up to appox. –280 kcal/mol, while the only lacunar β-[Mo$_8$O$_{26}$]$^{4-}$ anion exhibits the most negative sites (–290.5 kcal/mol) associated with the lacunae. The obtained data validated our hypothesis that the interactions with the lacunae of β-[Mo$_8$O$_{26}$]$^{4-}$ are more preferrable from both electrostatic and geometrical viewpoints than iodonium interactions with the other sites in the non-lacunar anions (for detailed discussion see **section 2.5**).
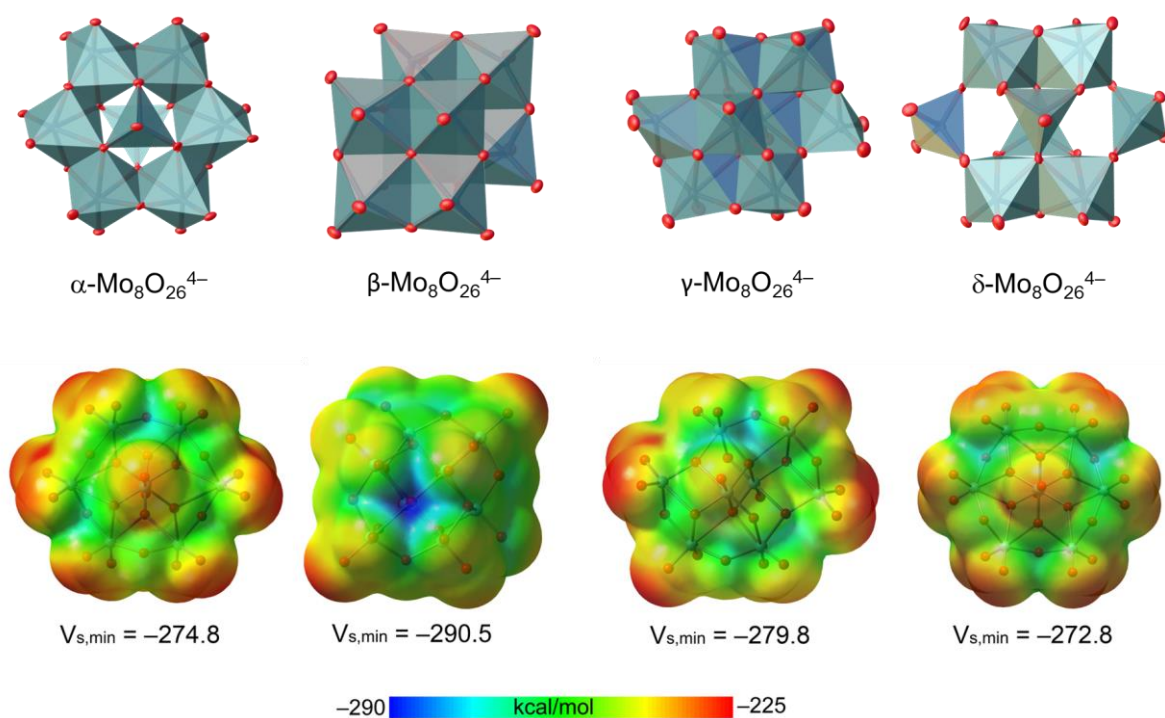

α-Mo$_8$O$_{26}$$^{4-}$	β-Mo$_8$O$_{26}$$^{4-}$	γ-Mo$_8$O$_{26}$$^{4-}$	δ-Mo$_8$O$_{26}$$^{4-}$
$V_{s,min}$ = –274.8	$V_{s,min}$ = –290.5	$V_{s,min}$ = –279.8	$V_{s,min}$ = –272.8

–290 ▬ kcal/mol ▬ –225

Figure S8. MEP surface (isodensity 0.001 a.u.) of [Mo$_8$O$_{26}$]$^{4-}$ isomers. The MEP minimum values are given in kcal/mol.

Table S2. Crystal data and structure refinement.

Identification code	1	2	3	4	5
CCDC number	2334362	2334363	2334360	2334364	2334361
Empirical formula	$C_{79.8}H_{106.2}N_{2.6}O_{28.6}Mo_8I_4$	$C_{52}H_{52}O_{28}S_2Mo_8I_4$	$C_{54}H_{54}N_2O_{28}Mo_8I_4$	$C_{64}H_{108}O_{26}Mo_8I_2N_2$	$C_{68}H_{118}N_2O_{27}Mo_8I_2$
Formula weight	2834.59	2464.17	2454.11	2342.84	2416.96
Temperature/K	150(2)	150(2)	150(2)	150(2)	150(2)
Crystal system	triclinic	triclinic	triclinic	monoclinic	monoclinic
Space group	P–1	P–1	P–1	P2$_1$/c	P2$_1$/c
a/Å	13.9442(4)	13.0495(3)	12.7533(3)	15.7278(3)	15.9198(3)
b/Å	14.7482(4)	14.4726(3)	12.7583(3)	16.3027(3)	19.5787(4)
c/Å	14.7605(4)	20.8666(5)	13.1803(3)	18.7455(3)	14.9460(3)
α/°	61.0800(10)	100.4640(10)	69.875(2)	90	90
β/°	81.7340(10)	98.6000(10)	64.408(2)	110.5660(10)	98.520(2)
γ/°	65.7040(10)	115.2890(10)	68.367(2)	90	90
Volume/Å^3	2415.85(12)	3387.69(14)	1753.71(8)	4500.13(14)	4607.09(16)
Z	1	2	1	2	2
ρ_{calc}g/cm^3	1.948	2.416	2.324	1.729	1.742
μ/mm^{-1}	2.355	3.396	3.223	1.829	1.790
F(000)	1380.0	2336.0	1164.0	2312.0	2396.0
Crystal size/mm^3	0.12 × 0.1 × 0.06	0.15 × 0.1 × 0.07	0.3 × 0.2 × 0.1	0.1 × 0.1 × 0.08	0.3 × 0.2 × 0.1
Radiation	MoKα (λ = 0.71073)	MoKα (λ = 0.71073)	MoKα (λ = 0.71073)	MoKα (λ = 0.71073)	MoKα (λ = 0.71073)
2Θ range for data collection/°	5.404 to 57.422	4.068 to 59.194	3.666 to 58.098	4.878 to 61.076	4.16 to 58.382

Index ranges	$-18 \le h \le 18$, $-19 \le k \le 19$, $-19 \le l \le 19$	$-18 \le h \le 18$, $-20 \le k \le 20$, $-28 \le l \le 28$	$-17 \le h \le 17$, $-15 \le k \le 17$, $-16 \le l \le 15$	$-21 \le h \le 22$, $-23 \le k \le 21$, $-26 \le l \le 26$	$-20 \le h \le 19$, $-26 \le k \le 26$, $-15 \le l \le 19$
Reflections collected	35741	54964	16766	83912	24632
Independent reflections	12209 [R_{int} = 0.0270, R_{sigma} = 0.0310]	18461 [R_{int} = 0.0310, R_{sigma} = 0.0366]	7792 [R_{int} = 0.0222, R_{sigma} = 0.0351]	13758 [R_{int} = 0.0369, R_{sigma} = 0.0275]	10435 [R_{int} = 0.0197, R_{sigma} = 0.0276]
Data/restraints/parameters	12209/1/563	18461/0/863	7792/0/439	13758/0/463	10435/0/495
Goodness–of–fit on F^2	1.042	1.065	1.040	1.050	1.058
Final R indexes [I>=2σ (I)]	R_1 = 0.0259, wR_2 = 0.0636	R_1 = 0.0306, wR_2 = 0.0694	R_1 = 0.0304, wR_2 = 0.0740	R_1 = 0.0225, wR_2 = 0.0464	R_1 = 0.0273, wR_2 = 0.0741
Final R indexes [all data]	R_1 = 0.0296, wR_2 = 0.0654	R_1 = 0.0401, wR_2 = 0.0720	R_1 = 0.0417, wR_2 = 0.0780	R_1 = 0.0311, wR_2 = 0.0479	R_1 = 0.0343, wR_2 = 0.0767
Largest diff. peak/hole / e Å^{-3}	0.82/–0.71	2.55/–1.47	2.45/–0.94	0.43/–0.48	2.52/–1.03

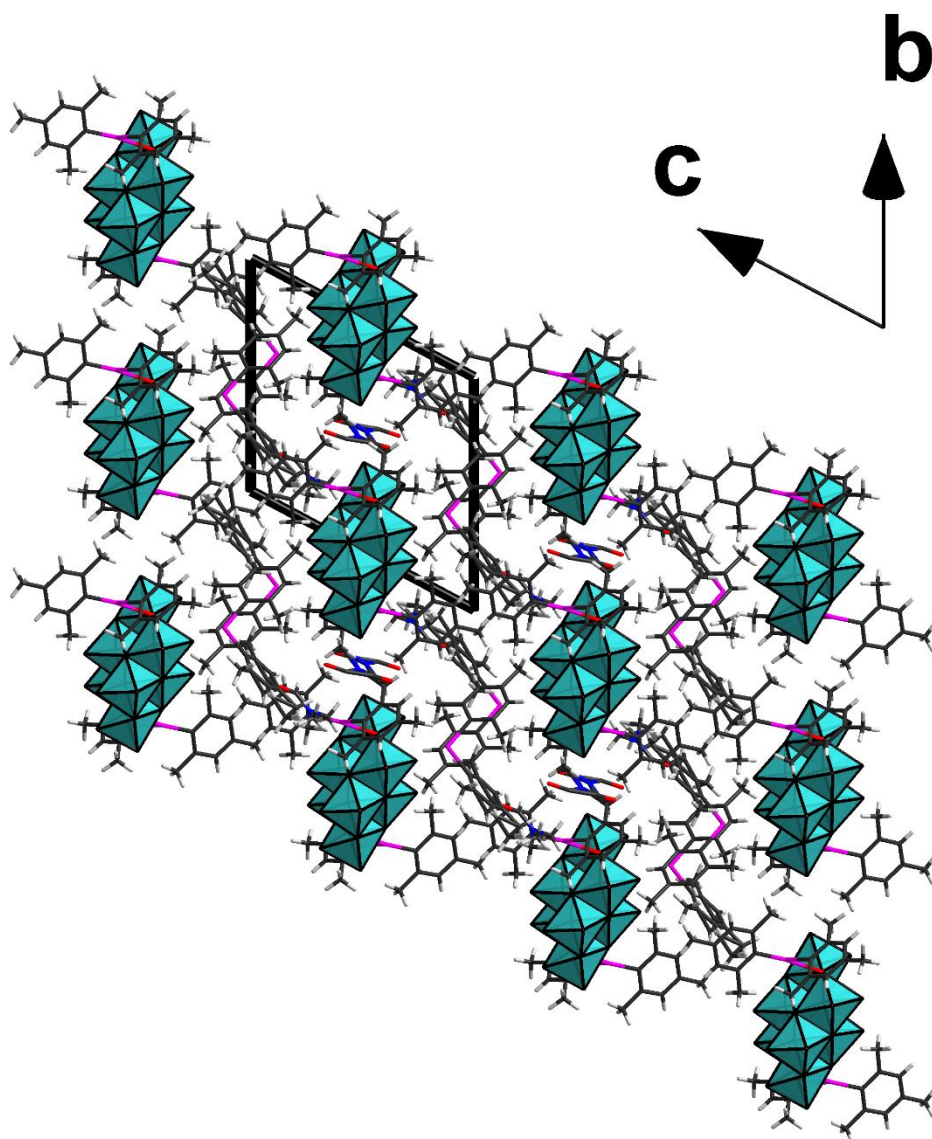## Section S5. Crystal packing of 1–5

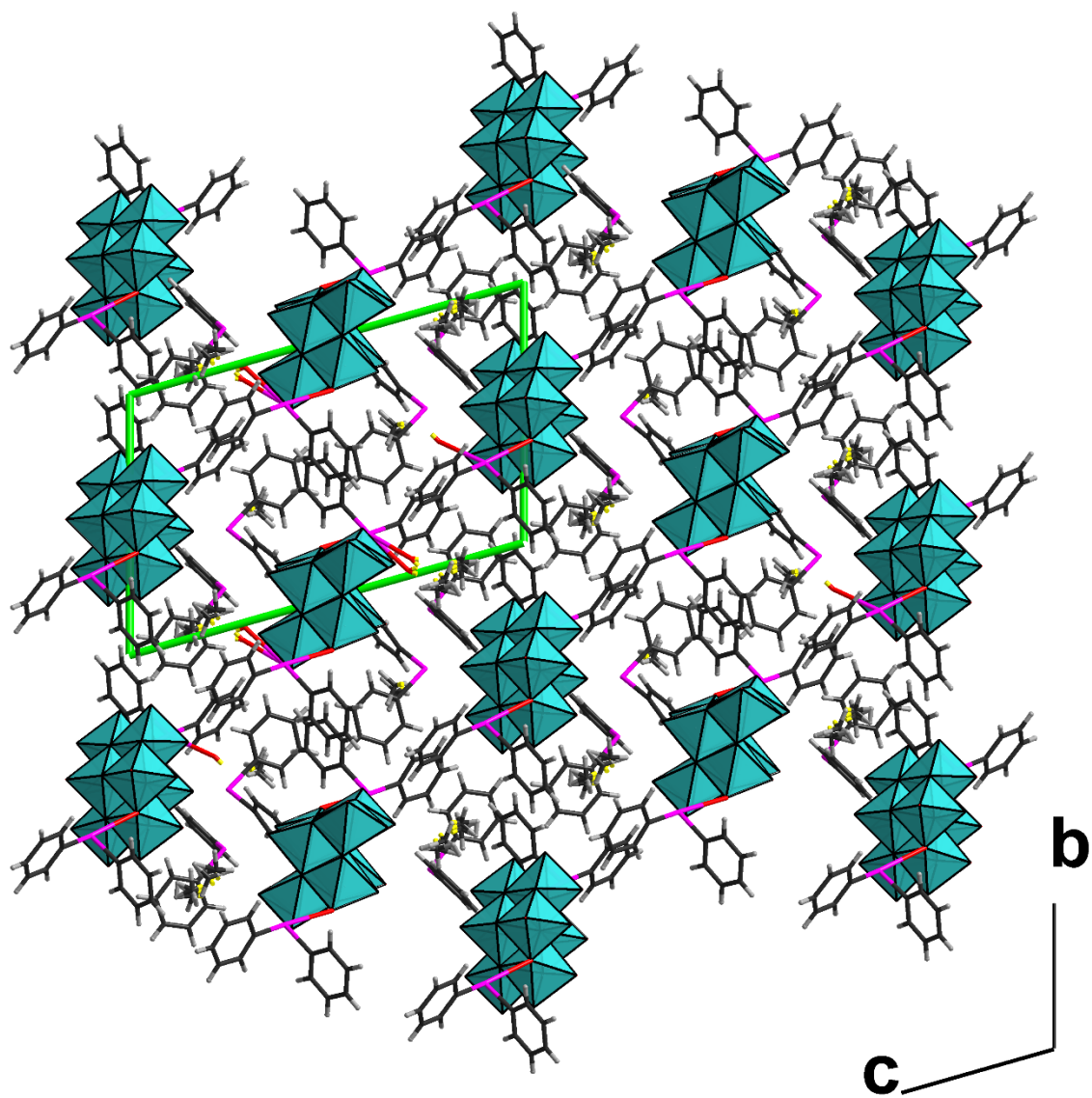**Figure S9.** Crystal packing of **1** along [100] crystal direction.

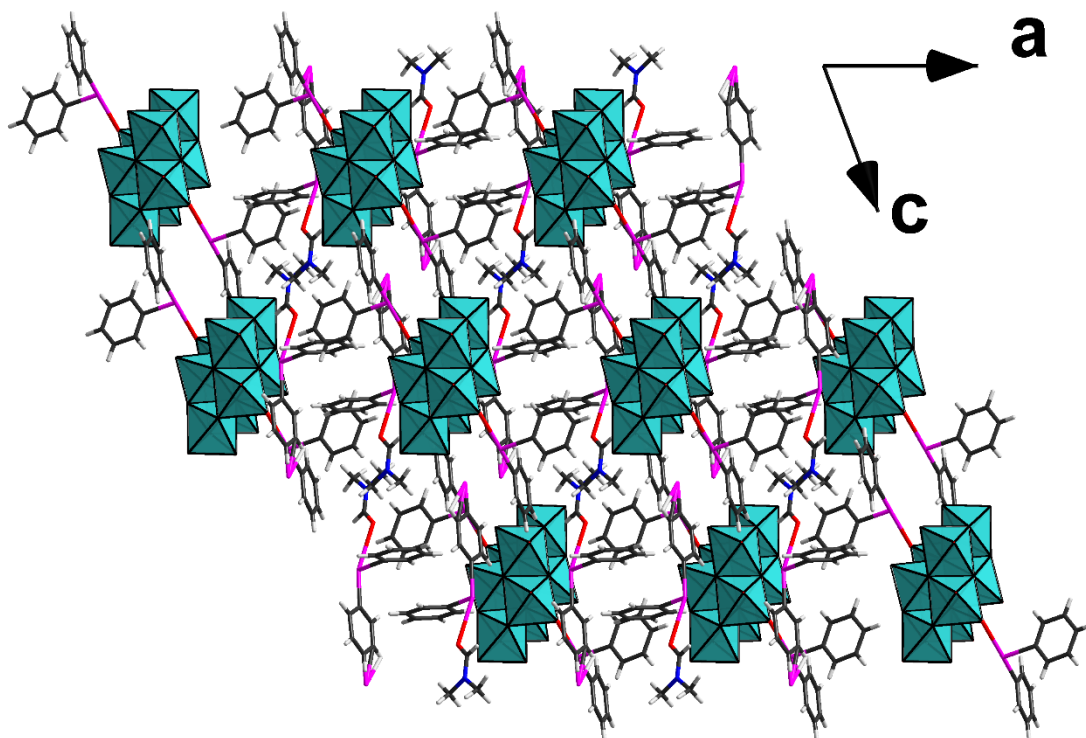**Figure S10.** Crystal packing of **2** along [100] crystal direction.

Figure S11. Crystal packing of **3** along [010] crystal direction.
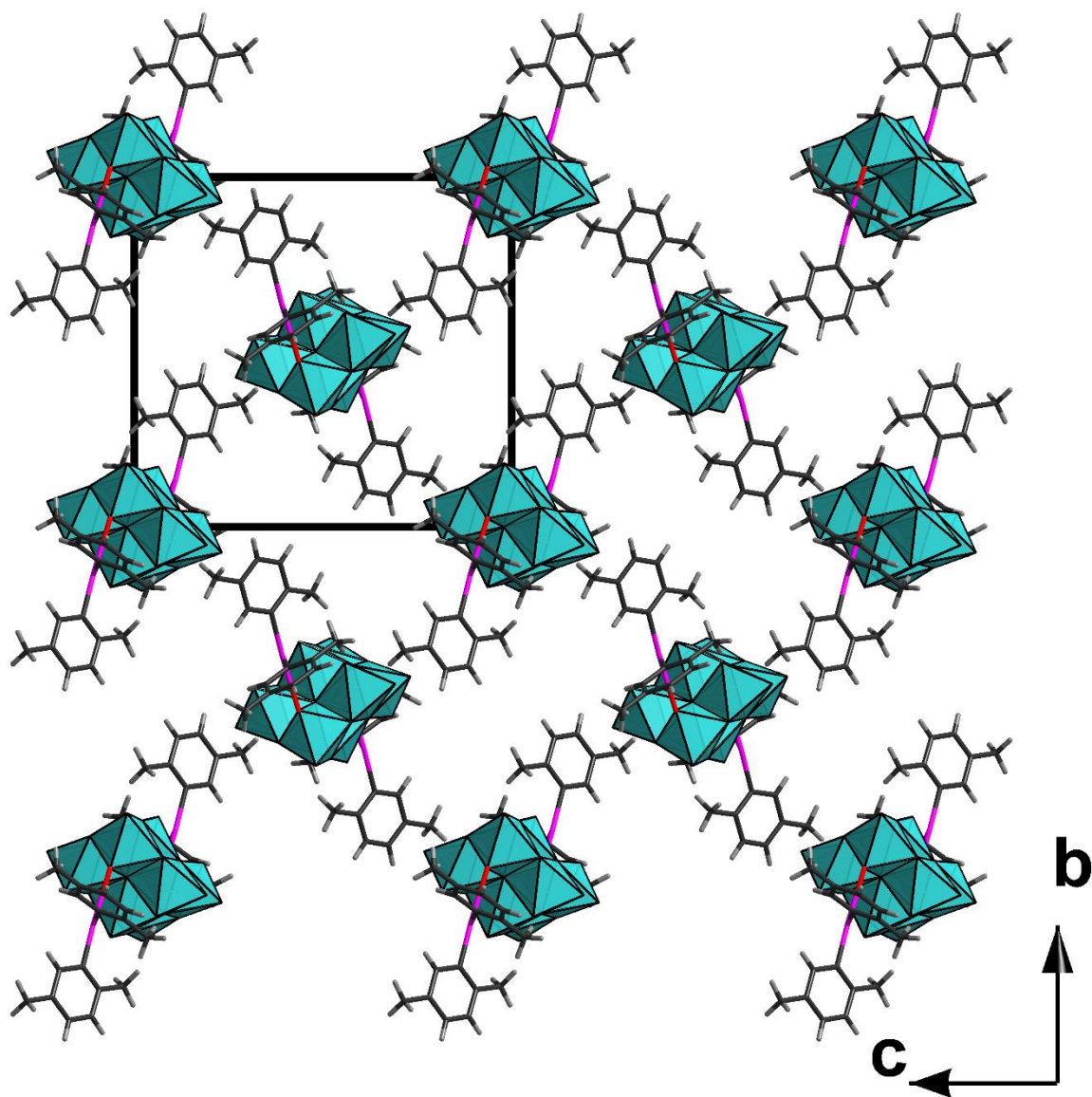
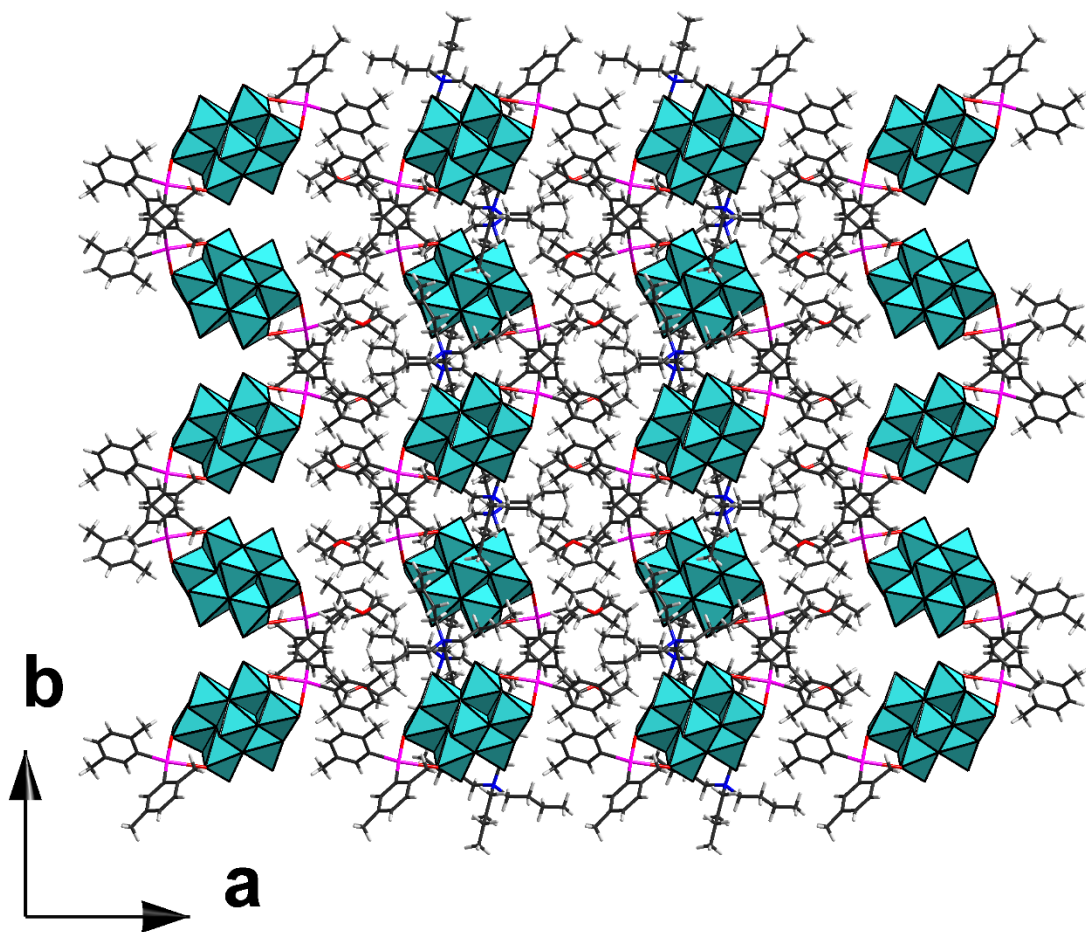**Figure S12.** Crystal packing of **4** along [100] crystal direction.

Figure S13. Crystal packing of **5** along [001] crystal direction.

Section S6. Synthetic work and crystal growth

$(Mes_2I)_4[Mo_8O_{26}] \cdot 2.6DMF$ (**1**). $(n\text{-}Bu_4N)_4[\beta\text{-}Mo_8O_{26}]$ (100 mg, 0.046 mmol) was dissolved in freshly distilled DMF (2 mL) under ultrasonic treatment and stirring, whereupon the solid compound $(Mes_2I)CF_3SO_3$ (95 mg, 0.184 mmol) was added. The mixture was placed in a desiccator in Et_2O atmosphere at 5 °C and after 1 d a crop of released block colorless crystals was separated by filtration. The crude product was washed with Et_2O (2 × 6 mL) and dried in air at room temperature to give **1** as the colorless crystalline solid (90 mg, 69%). The phase purity was confirmed by XRPD (**Section S6**, the ESI). Elemental analyses: Calc. for $C_{79.8}H_{106.2}I_4Mo_8N_{2.6}O_{28.6}$ C, H, N (%): 33.8, 3.8, 1.3. Found C, H, N (%): 33.7, 3.9, 1.5. IR (KBr, selected bands, cm^{-1}): 914 $\nu(Mo=O)$, 902 $\nu(Mo=O)$, 841 $\nu(Mo-O-Mo)$, 729 $\nu(Mo-O-Mo)$, 708 $\nu(Mo-O-Mo)$, 657 $\nu(C-I)$.

$(Ph_2I)_4[Mo_8O_{26}] \cdot 2DMSO$ (**2**): $(n\text{-}Bu_4N)_4[\beta\text{-}Mo_8O_{26}]$ (100 mg, 0.046 mmol) was dissolved in freshly distilled DMSO (2 mL) under ultrasonic treatment and stirring, whereupon the solid compound $(Ph_2I)CF_3SO_3$ (80 mg, 0.184 mmol) was added. The mixture was placed in a desiccator in ^iPrOH atmosphere at room temperature and after 3 d a crop of block colorless crystals was separated by filtration. The crude product was washed with Et_2O (2 × 6 mL) and dried in air at room temperature to give **2** as the colorless crystalline solid (101 mg, 91%). The phase purity was confirmed by XRPD (**Section S6**, the ESI). Elemental analyses: Calc. for $C_{52}H_{52}I_4Mo_8O_{28}S_2$ C, H, S (%): 25.4, 2.1, 2.6. Found C, H, S (%): 25.4, 2.2, 2.7. IR (KBr, selected bands, cm^{-1}): 908 $\nu(Mo=O)$, 893 $\nu(Mo=O)$, 842 $\nu(Mo-O-Mo)$, 705 $\nu(Mo-O-Mo)$, 652 $\nu(C-I)$.

$(Xyl_2I)_2(n\text{-}Bu_4N)_2[Mo_8O_{26}]$ (**4**): $(n\text{-}Bu_4N)_4[\beta\text{-}Mo_8O_{26}]$ (100 mg, 0.046 mmol) was dissolved in freshly distilled DMSO (2 mL) under stirring and ultrasonic treatment, whereupon the solid compound $(Xy_2I)CF_3SO_3$ (80 mg, 0.184 mmol) was added. The mixture was placed in a desiccator in ^iPrOH atmosphere at room temperature. Th released monophase crystals after 1 d were separated by filtration; longer storage of these crystals in the mother liquor led to their phase contamination. The separated crystals were washed consequently with ^iPrOH (2 × 6 mL) and Et_2O (2 × 6 mL) and dried in air at room temperature to give **4** as the colorless crystalline solid (80 mg, 74%). In contrast to the studied single-crystal of **4**, which contain DMSO of solvation, the isolated product does not contain DMSO, which was lost during the isolation. The phase purity of the single-crystals and the isolated product was confirmed by XRPD (**Section S6**, the ESI). Elemental

analyses: Calc. for $C_{64}H_{108}I_2Mo_8N_2O_{26}$ C, H, N (%): 32.8, 4.6, 1.2. Found C, H, N (%): 32.8, 4.6, 1.6. IR (KBr, selected bands, cm^{-1}): 910 ν(Mo=O), 896 ν(Mo=O), 844 ν(Mo–O–Mo), 732 ν(Mo–O–Mo), 708 ν(Mo–O–Mo), 658 ν(C–I).

(Ph$_2$I)$_4$[Mo$_8$O$_{26}$]·2DMF (**3**) and (Xyl$_2$I)$_2$(n-Bu$_4$N)$_2$[Mo$_8$O$_{26}$]·Et$_2$O (**5**) were prepared and isolated similar to the procedure developed for **1**. According to the XRPD data, the phase composition is different depending on (R$_2$I)$^+$/n-Bu$_4$N$^+$ ratios.

Section S7. Powder XRD pattern of 1, 2, and 4
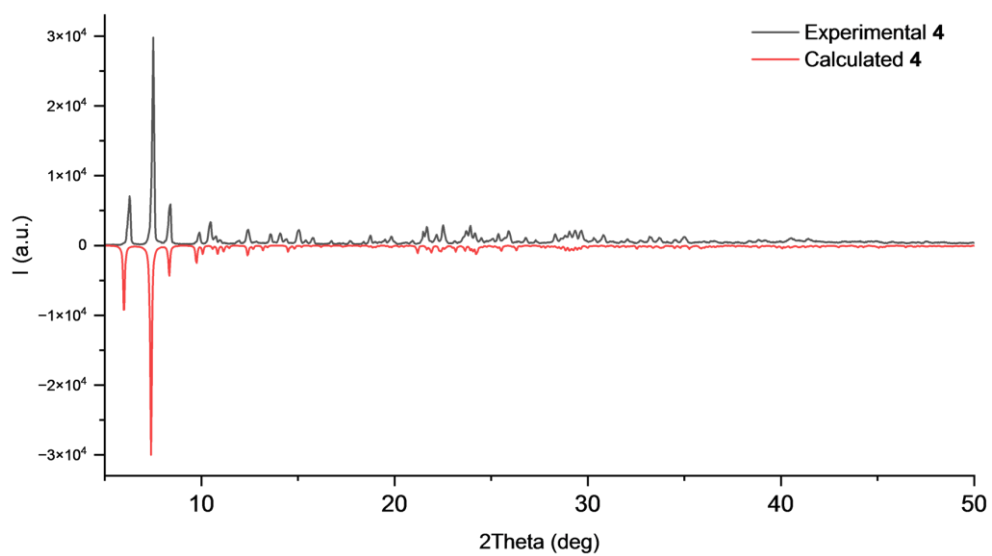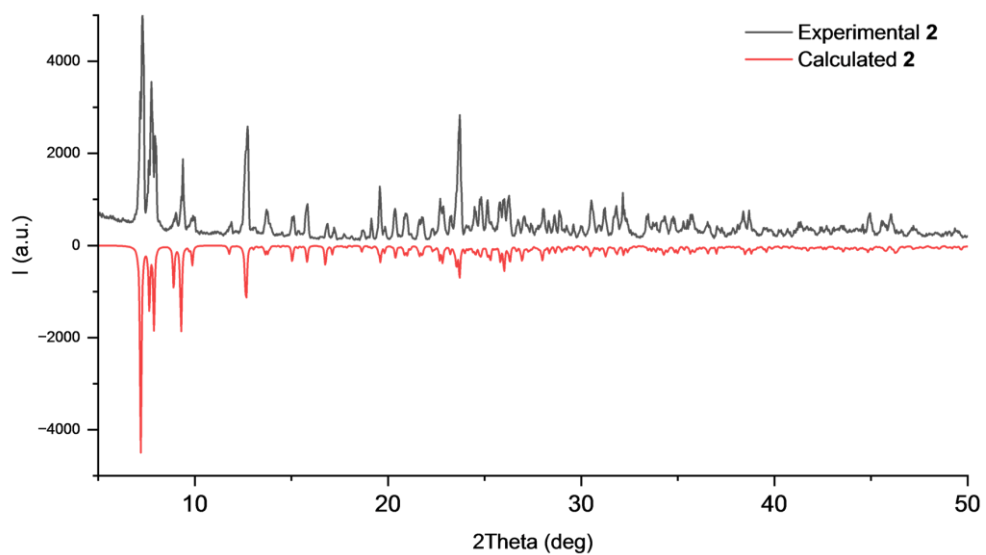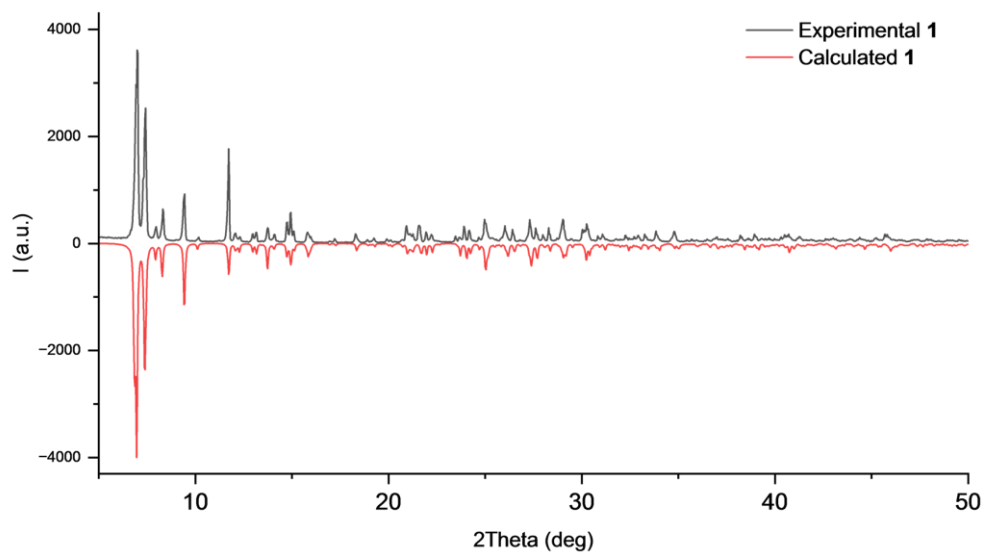
Section S8. FTIR spectra of 1, 2, and 4
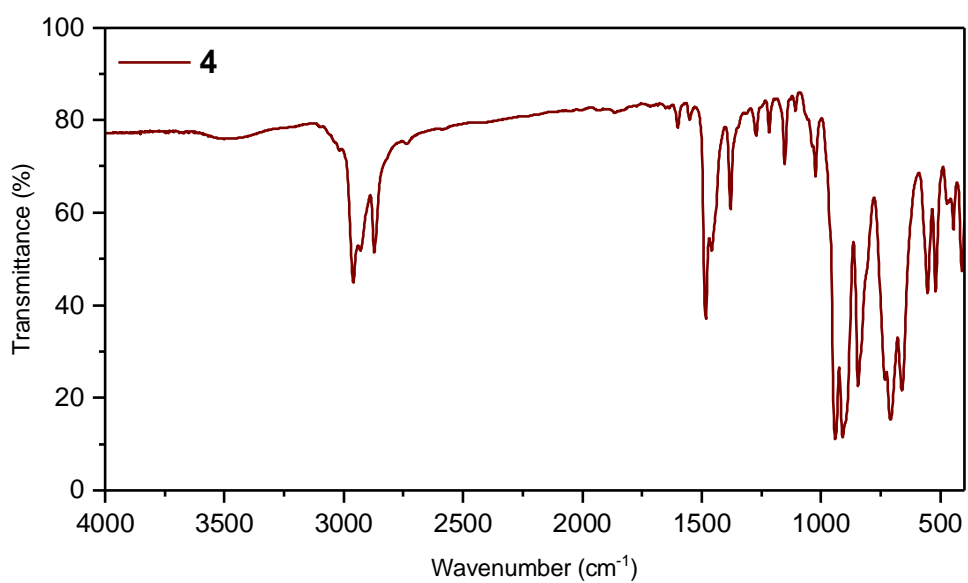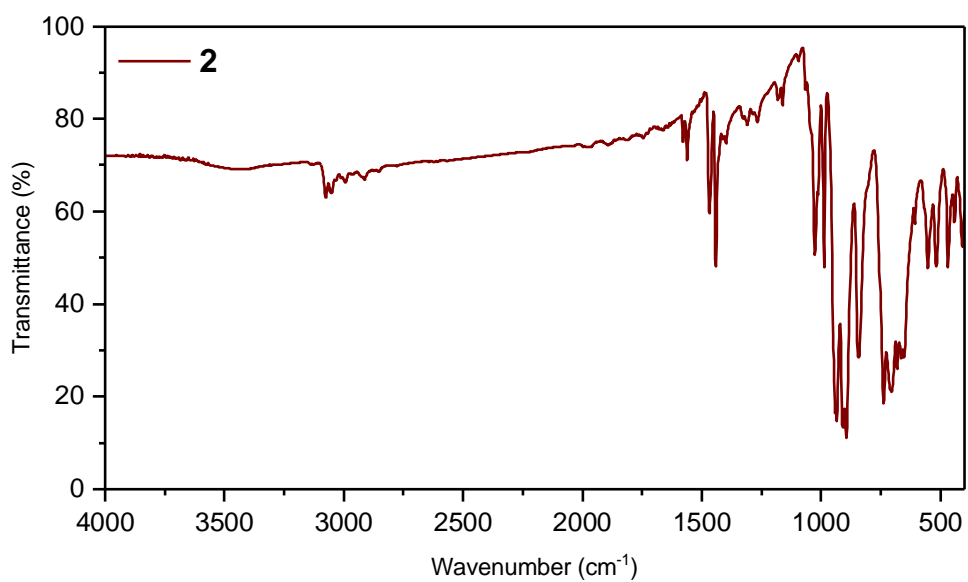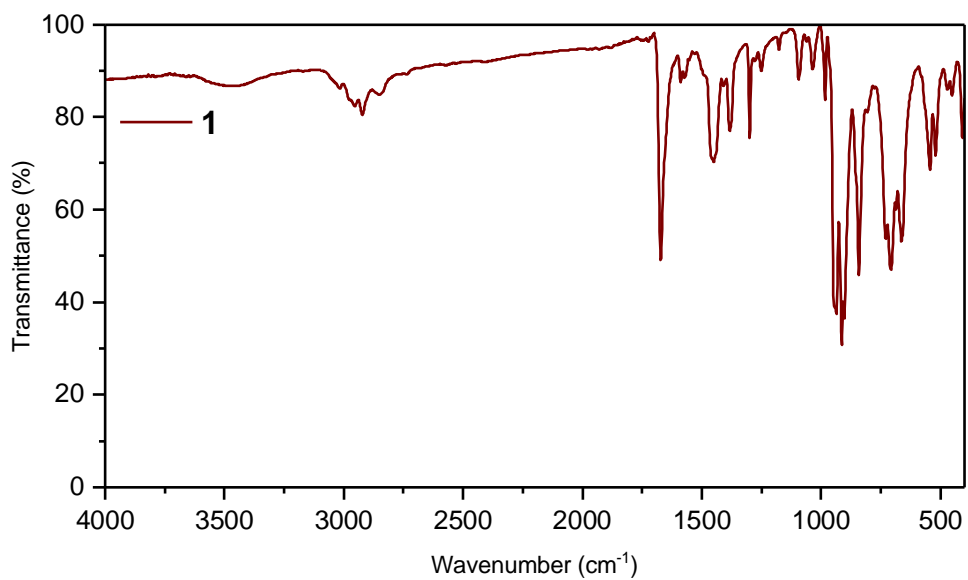
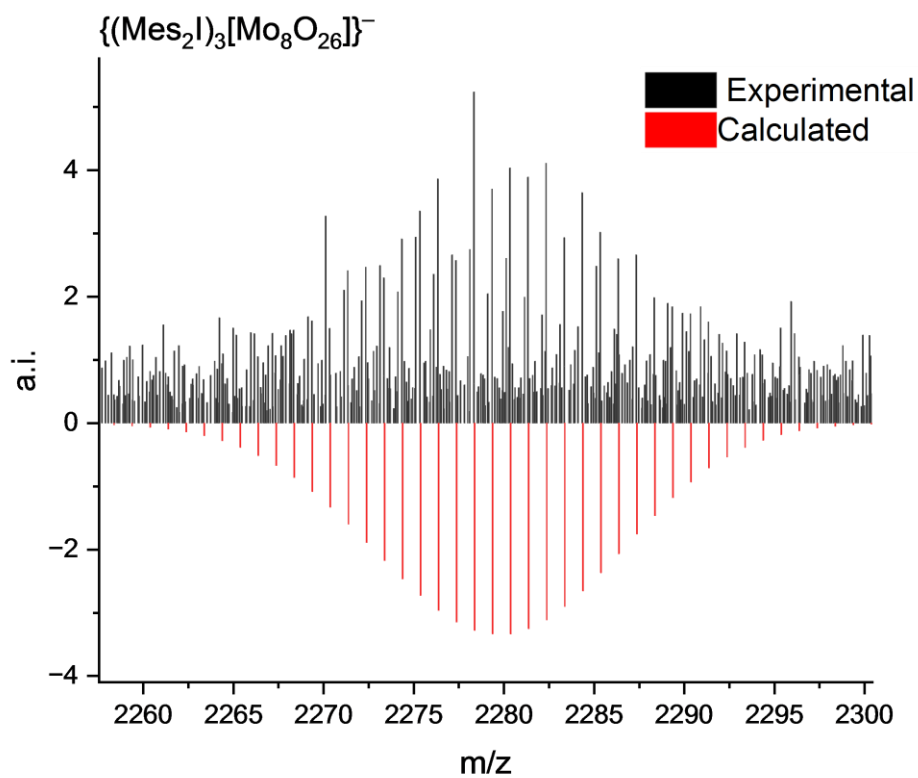# Section S9. High resolution mass spectrometry of 1, 2 and 4

$\{(Mes_2I)_3[Mo_8O_{26}]\}^-$

Table S3. ESI-MS spectra assignments for compound **1**.

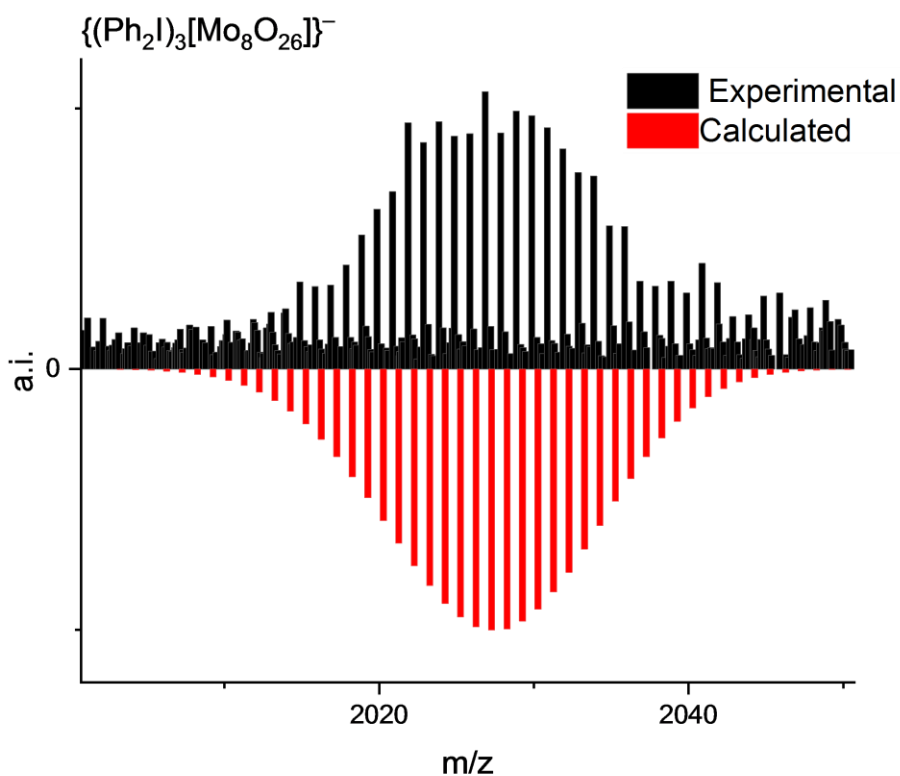| Species	Charge mode	Chemical Formula	Calculated, m/z	Found, m/z
$\{(Mes_2I)_3[Mo_8O_{26}]\}^-$	Negative	$C_{54}H_{66}I_3Mo_8O_{26}^-$	2294.3414	2294.3467
Mes_2I^+	Positive	$C_{18}H_{22}I^+$	365.0761	365.0768

$\{(Ph_2I)_3[Mo_8O_{26}]\}^-$

Table S4. ESI-MS spectra assignments for compound **2**.

Species	Charge mode	Chemical Formula	Calculated, m/z	Found, m/z
$\{(Ph_2I)_3[Mo_8O_{26}]\}^-$	Negative	$C_{36}H_{30}I_3Mo_8O_{26}^-$	2042.0597	2042.0606
Ph_2I^+	Positive	$C_{12}H_{10}I^+$	280.9822	280.9819

$\{(Xyl_2I)_2(n\text{-}Bu_4N)[Mo_8O_{26}]\}^-$
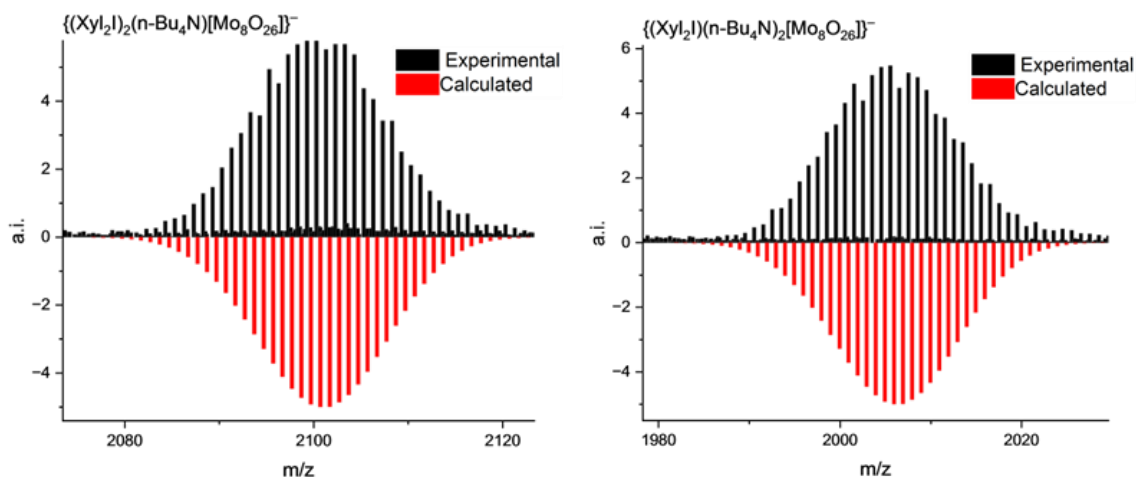

$\{(Xyl_2I)(n\text{-}Bu_4N)_2[Mo_8O_{26}]\}^-$

Table S5. ESI-MS spectra assignments for compound **4**.

Species	Charge mode	Chemical Formula	Calculated, m/z	Found, m/z
$\{(Xyl_2I)_2(n\text{-}Bu_4N)[Mo_8O_{26}]\}^-$	Negative	$C_{48}H_{72}I_2Mo_8NO_{26}^-$	2115.487	2210.4850

{(Xyl₂I)(n-Bu₄N)₂[Mo₈O₂₆]}⁻	Negative	$C_{48}H_{90}IMo_8N_2O_{26}^-$	2020.7265	2020.7343
Xyl_2I^+	Positive	$C_{16}H_{18}I^+$	337.0448	337.0451
$n\text{-}Bu_4N^+$	Positive	$C_{16}H_{36}N^+$	242.2842	242.2841

References

1   L. Fotović, N. Bedeković and V. Stilinović, *Cryst. Growth Des.*, 2023, **23**, 3384–3392.

2   A. V. Chupina, V. Shayapov, A. S. Novikov, V. V. Volchek, E. Benassi, P. A. Abramov and M. N. Sokolov, *Dalt. Trans.*, 2020, **49**, 1522–1530.

3   L.-S. Wang, Y. Lu, G. M. Ó. Máille, S. P. Anthony, D. Nolan and S. M. Draper, *Inorg. Chem.*, 2016, **55**, 9497–9500.

4   J. Li, Y. Zhao, B. Huang, Y. Wang, Z. Xiong, B. Xiao, Y. Zhao, Z. Xiao and P. Wu, *J. Clust. Sci.*, 2022, **33**, 2375–2381.

5   D. Kuriakose and M. R. Prathapachandra Kurup, *Inorganica Chim. Acta*, 2020, **505**, 119472.

6   D. Kuriakose and M. R. P. Kurup, *Polyhedron*, 2019, **170**, 749–761.

7   M. Oszajca, Ľ. Smrčok and W. Łasocha, *Acta Crystallogr. Sect. C Cryst. Struct. Commun.*, 2013, **69**, 1367–1372.

8   C. B. Aakeroy, D. L. Bryce, G. R. Desiraju, A. Frontera, A. C. Legon, F. Nicotra, K. Rissanen, S. Scheiner, G. Terraneo, P. Metrangolo and G. Resnati, *Pure Appl. Chem.*, 2019, **91**, 1889–1892.

9   I. I. Fedorova, N. S. Soldatova, D. M. Ivanov, K. Nikiforova, I. S. Aliyarova, M. S. Yusubov, P. M. Tolstoy, R. M. Gomila, A. Frontera, V. Y. Kukushkin, P. S. Postnikov and G. Resnati, *Cryst. Growth Des.*, 2023, **23**, 2661–2674.

10   X. L. Wang, J. Y. Zhang, Z. H. Chang, Z. Zhang, X. Wang, H. Y. Lin and Z. W. Cui, *Inorg. Chem.*, 2021, **60**, 3331–3337.